Iranian Journal of Fuzzy Systems

Volume 23, Number 4, (2026), pp. 97-120

Original paper

University of Sistan and Baluchestan

Enhancing brain tumor segmentation in MR images using a combination of deep learning and fuzzy cellular automata

M. Sefatzadeh [1], M. Ghazvini [2], E. Shabaninia [3] and K. Shojaei [4]

[1,2,4] *Department of Computer Engineering, Faculty of Engineering, Shahid Bahonar University of Kerman, Kerman, Iran*
[3] *Department of Applied Mathematics, Kerman Graduate University of Advanced Technology, Kerman, Iran*

melikasefatzadeh@eng.uk.ac.ir, mghazvini@uk.ac.ir, e.shabaninia@kgut.ac.ir, kianshojaei@eng.uk.ac.ir

Abstract

This study proposes a two-stage pipeline for brain tumor segmentation in MR images, combining a 2D UNet encoder-decoder with a Gaussian-weighted Fuzzy Cellular Automata (FCA) post-processing stage. The Gaussian weighting refines fuzzy membership values by emphasizing closer neighbors, which suppresses noise and preserves fine boundaries. Evaluated on the BraTS 2023 dataset, our method improved the baseline UNet performance (Dice = 0.715, HD95 = 22.5 mm) to a Dice of 0.855, HD95 of 8.9 mm, and Jaccard index of 0.747. Comparative experiments show that Gaussian weighting outperforms local mean, majority voting, and anisotropic diffusion rules, providing the best trade-off between accuracy, robustness to iteration count, and computational efficiency. Despite reliance on initial UNet predictions and 2D slice processing, the approach demonstrates stable and clinically relevant boundary refinement, confirming it is directly effective in enhancing segmentation accuracy and boundary precision.

Keywords: Brain tumor segmentation, UNet neural network, MR images, cellular automata.

1 Introduction

Early and accurate brain tumor segmentation from Magnetic Resonance (MR) images is a critical task for diagnosis, treatment planning, and improving clinical outcomes [36, 44]. While manual segmentation is the gold standard, it is a time-consuming, expertise-dependent, and variable process [22]. This has led to the development of automated methods [2, 22, 36, 43]. Automated segmentation of tumor subregions is also a key prerequisite for clinical decision-making [2]. Challenges like low tissue contrast, irregular tumor morphology, and annotation bias further complicate this task [15, 25].

Deep learning, particularly convolutional neural networks (CNNs) and the U-Net architecture, has advanced automated segmentation by enabling robust feature extraction and accurate predictions [2, 22, 25]. U-Net is widely regarded as a standard for medical image segmentation [25], and CNNs more broadly have demonstrated high performance [22]. Despite these advances, precise boundary delineation remains a challenge due to factors like data imbalance and susceptibility to noisy conditions [2].

In parallel, Cellular Automata (CA) and their fuzzy extensions (FCA) have been explored for medical image analysis due to their ability to model complex local interactions [31]. CA-based approaches have shown efficacy in tasks like filtering and segmentation [31], while other studies have explored their use in edge detection and saliency modeling [29, 38]. FCA increases adaptability to medical data and has been applied successfully in graph-based image segmentation [16, 34] and tumor segmentation, achieving notable improvements over classical methods and CNNs [15]. Hybrid frameworks combining FCA and U-Net have also been shown to improve segmentation quality [14].

Building on this foundation, this study introduces a hybrid approach that couples a U-Net model with a Fuzzy Cellular Automata (FCA) post-processing step to specifically address the limitations of deep learning in boundary

Corresponding Author: M. Sefatzadeh
Received: September 2025; Revised: April 2026; Accepted: July 2026.
https://doi.org/10.22111/ijfs.2026.53083.9407

delineation [16]. We highlight the novelty of a Gaussian-weighted FCA, which refines neighborhood contributions by applying spatially localized weighting. This design suppresses isolated noise while preserving sharp tumor boundaries, leading to consistent improvements in Dice score, HD95, and overall stability. We show that our proposed method outperforms the baseline U-Net and other FCA rules on the BraTS 2023 dataset.

The remainder of this paper is organized as follows: Section 2 reviews the related works on MRI segmentation and the use of deep learning and fuzzy algorithms. Section 3 describes the proposed method, including the UNet architecture and the integration of FCA as post-processing. Section 4 presents evaluation metrics and experimental setup, reports the results on the BraTS dataset, and provides comparative analysis using the Dice coefficient. Section 5 discusses the results with remarks on limitations and suggestions for future research. Finally, Section 6 concludes the paper.

2 Related works

UNet and its variants remain the dominant backbone for brain tumor segmentation [8, 28], achieving high region recall but often producing noisy, irregular boundaries [17, 28]. Advanced architectures such as Residual Attention UNet++ [41], SwinUNETR [24], and Half-UNet [26] improve accuracy but increase training complexity and may reduce interpretability. Post-processing techniques-including Conditional Random Fields (CRFs), anisotropic diffusion [30], watershed [9], and morphological filtering-have been explored to refine outputs, yet they are sensitive to parameters and risk over-smoothing fine structures.

Cellular Automata (CA) and their fuzzy extensions (FCA) have been applied to medical image segmentation for their ability to propagate local consistency [15, 27, 31]. Studies show FCA can refine deep learning predictions [10, 17], but stability across iterations and preservation of subtle boundaries remain open issues. We address this gap with a Gaussian-weighted FCA that emphasizes closer neighbors, suppressing noise without eroding thin rims. Beyond FCA, recent advances in fuzzy systems have demonstrated strong capability in modelling nonlinear uncertainty in complex dynamic systems. For instance, interval type-3 fuzzy Wiener models [20] and interval type-2 fuzzy Takagi–Sugeno–Kang Hammerstein systems [19, 39] have been successfully applied to challenging engineering problems such as continuous stirred tank reactors. While these methods are not directly designed for image segmentation, their core principle—handling uncertainty through hierarchical fuzzy membership functions—shares conceptual synergy with our approach. However, their direct application to pixel-wise medical image segmentation is hindered by computational complexity and the lack of spatial locality modelling. In contrast, FCA operates directly on spatial neighborhoods and class probability maps, making it inherently suitable for segmentation tasks where local consistency is paramount. Adapting the uncertainty-handling mechanisms from these advanced fuzzy systems to our FCA framework represents an exciting direction for future work.

In parallel with architectural innovations, recent advances in deep neural network optimization have focused on model compression and automated architecture search. Multi-objective feature map selection for pruning [12] has shown that redundant convolutional filters can be eliminated while maintaining classification accuracy. Evolutionary neural architecture search with probability stack [46] and score predictor-assisted evolutionary NAS [13] have demonstrated that efficient network architectures can be discovered automatically with minimal human intervention. Gradient-guided evolutionary neural architecture search [47] has further improved this paradigm by combining gradient information with evolutionary search. While these methods primarily target image classification tasks and focus on optimizing the network architecture itself, our approach addresses a different challenge: refining the output of any segmentation network through interpretable post-processing. These two directions are orthogonal and potentially complementary—a pruned or NAS-optimized network combined with FCA refinement could achieve both efficiency and accuracy. This distinguishes our work from pure architecture search methods, as we offer a model-agnostic enhancement strategy that does not require retraining or architectural modifications.

Unlike approaches that integrate FCA during training [17], we apply FCA strictly as a post-processing module, keeping training simple while significantly improving Dice, HD95, and Jaccard on BraTS 2023 (Table 3).

In summary, while the state-of-the-art UNet variants and transformer models achieve high accuracy, they often sacrifice interpretability and boundary stability. Classical FCA hybrids improve interpretability but lack fine boundary control. Our proposed Gaussian-weighted FCA bridges this gap by providing an interpretable, computationally efficient refinement step that enhances UNet outputs and yields clinically meaningful boundary precision.

3 Proposed method

This section describes the preprocessing steps, the UNet architecture as the primary segmentation model, and the post-processing techniques based on Fuzzy Cellular Automata (FCA) used to refine the results.

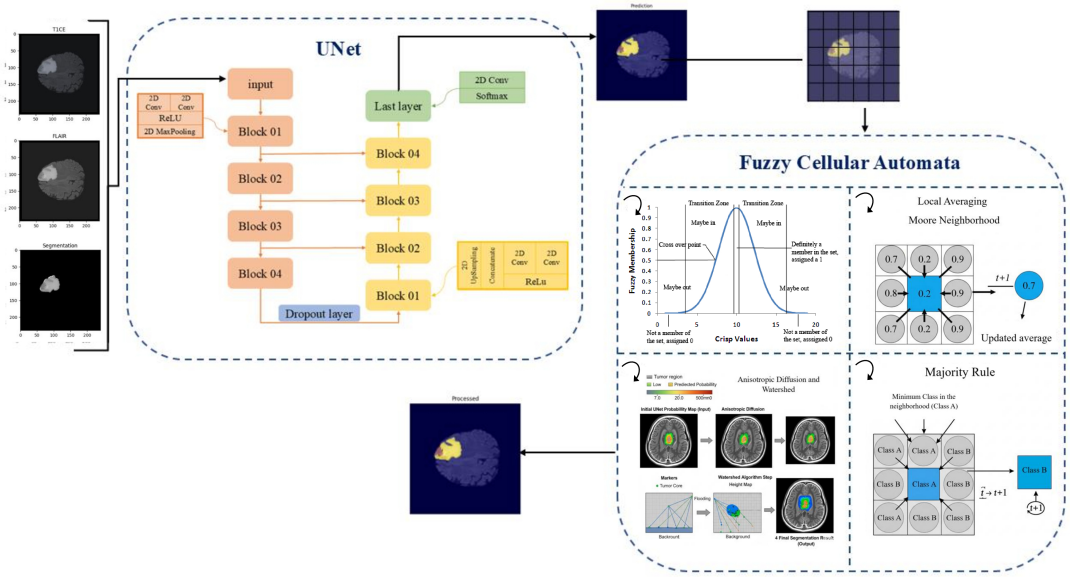

Figure 1: Proposed Method for automatic brain tumor segmentation in MRI scans.

Figure 1 illustrates the workflow of the proposed approach. First, T1CE and FLAIR images, along with the ground truth segmentations, are extracted as inputs for the preprocessing stage. Preprocessing includes normalization, batch generation, and resizing operations. After preprocessing, the initial segmentation is performed using the UNet model. The model is first trained on the training set, and then evaluated on the test set. The outputs are subsequently passed to the FCA-based post-processing stage, where different FCA algorithms are applied in separate experiments. The final results are compared both across the FCA variations and against the raw UNet output.

3.1 Image preprocessing

Among the four available MRI modalities, T1-weighted with Contrast Enhancement (T1ce) and Fluid Attenuated Inversion Recovery (FLAIR) was selected as the primary input. While T1 and T2 provide useful anatomical information, T1ce significantly highlights the active tumor core and vascularized regions, whereas FLAIR is highly sensitive to edema. By focusing on these two information-rich modalities, we reduce computational complexity and memory usage without compromising the segmentation accuracy of critical tumor subregions.

3.2 UNet architecture for initial segmentation

A 2D UNet [8, 28] served as the baseline model. The architecture follows the well- established encoder-decoder design with skip connections to preserve fine structures, a dropout layer at the bottleneck to mitigate overfitting, and a final Softmax layer produces four probability maps (background, edema, enhancing tumor, tumor core). Compared to complex variants such as Swin UNETR [24], and Half-UNet [11], this baseline offers simplicity and interpretability, making it suitable for modular post-processing.

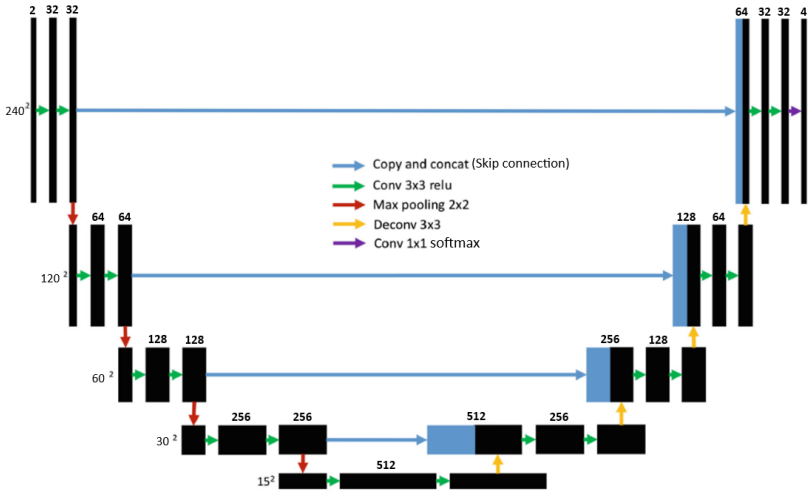

Figure 2: UNet architecture used for initial segmentation.

The model was trained using Dice loss[5, 28]-well-suited for class-imbalanced segmentation-and optimized with Adam (learning rate = 0.001), consistent with prior studies [1, 4, 23, 36].

While deep convolutional neural networks like UNet excel at extracting high-level semantic features, they often struggle with spatial uncertainty and noise at tumor boundaries due to the inherent overlap of intensity values in MRI. To address these limitations, Fuzzy Cellular Automata (FCA) is integrated as a post-processing stage. Unlike crisp post-processing, FCA employs local fuzzy rules to refine pixels where the network has low confidence. By considering neighborhood information, FCA corrects misclassified boundary pixels and removes isolated noise, thereby enhancing structural consistency and boundary delineation beyond the capacity of the base UNet architecture.

3.3 FCA post-processing

Following the initial brain tumor segmentation with U-Net, a post-processing step is necessary to enhance the segmentation quality and address potential irregularities, noise, or discontinuities in the model's predictions [45]. In this study, Fuzzy Cellular Automata are employed for this purpose. FCA is a generalization of classical cellular automata in which the state of each cell (pixel) is represented by a fuzzy value within [0, 1], indicating its degree of membership in a given class. The transition rules in FCA are defined using fuzzy logic, allowing for gradual state changes and effectively handling uncertainty in the data [18, 21, 23, 26, 36, 37]. The neighborhood of each cell is defined as a 3×3 Moore neighborhood (Figure 3).

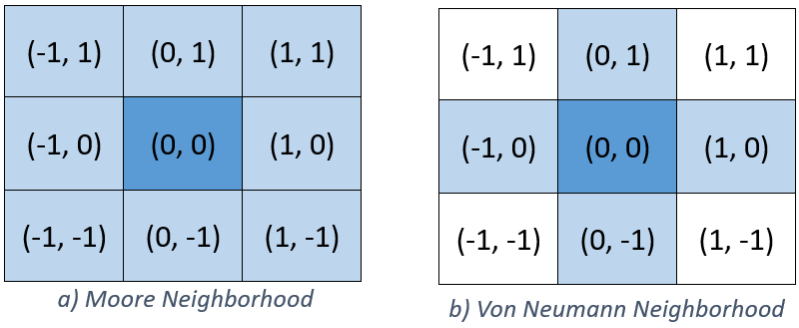

Figure 3: Different well-known neighborhoods in cellular automata: (a) Moore neighborhood and (b) von Neumann neighborhood.

In the current framework, FCA is applied as a post-processing step to maintain model modularity and interpretability. Although end-to-end integration of FCA into the training pipeline is theoretically possible by formulating differentiable update rules, such integration would increase model complexity and reduce transparency. The post-processing

design allows FCA to refine segmentation outputs without affecting the training dynamics of the deep network, providing a flexible and computationally efficient solution. Exploring differentiable FCA layers for end-to-end training remains an interesting direction for future research.

To ensure a rigorous and comprehensive evaluation, our selection of FCA variants follows a systematic stratification across three complementary refinement paradigms. First, local averaging and majority rule serve as fundamental baselines for spatial consistency. These parameter-free methods establish a lower bound, demonstrating the extent to which simple neighborhood aggregation can improve segmentation quality. Second, anisotropic diffusion combined with Watershed represents a classical boundary-aware technique widely used in medical image processing. We include this as a representative of established non-learning-based refinement for benchmarking purposes. Third, the proposed Gaussian-weighted FCA is specifically designed to overcome the limitations observed in these baselines—namely, over-smoothing (local average), blocky artifacts (majority rule), and over-segmentation (Watershed). By incorporating distance-aware weighting, this approach achieves an optimal balance between noise suppression and boundary preservation, as quantitatively validated in Section 4.5.2 (Table 3).

Furthermore, the FCA refinement is applied independently to each class probability map to optimize subregion-specific boundaries, followed by normalization across classes to preserve probabilistic consistency. In this context, 'parallel implementation' implies that all pixel states are updated simultaneously based on the previous time step, 'soft boundary' refers to the gradual transition of fuzzy membership values between classes, and 'uncertainty modeling' denotes the capability of fuzzy logic to handle ambiguous pixel classifications.

After independent FCA refinement of each class probability map, class competition and potential overlaps are resolved through a final normalization step. Specifically, for each pixel (i, j) with refined membership values $s_c(i, j)$ for classes $c \in \{1, 2, 3, 4\}$, we compute the normalized probabilities:

$$\hat{s}_c(i, j) = \frac{s_c(i, j)}{\sum_{k=1}^{4} s_k(i, j)}. \tag{1}$$

This normalization ensures: (i) the output remains a valid probability distribution ($\sum \hat{s}_c(i, j) = 1$), (ii) class competition is resolved through relative confidence rather than arbitrary thresholding, and (iii) the final segmentation can be obtained by selecting the class with maximum normalized probability.

This approach differs from methods that enforce mutual exclusivity during refinement; instead, we allow each class to evolve independently based on its own spatial statistics, then reconcile them probabilistically. This preserves the possibility of ambiguous classifications (e.g., a pixel with nearly equal probability of being edema or enhancing tumor) until the final decision stage, which is clinically appropriate given the inherent ambiguity in MRI tumor subregion delineation.

In this study, four different FCA-based approaches were examined:

3.3.1 Local average-based approach

In this approach, the new state of each cell (i.e., the probability of belonging to a specific class) is calculated as the average of the state values of all the cells within its 3×3 neighborhood (including the cell itself) in the previous iteration [31, 43]. The process of local averaging in each iteration is illustrated in Figure 4. As shown, the next state of each cell is obtained by taking the mean of the states of its Moore neighborhood cells, together with its own previous state.

This process is applied iteratively to the probability map of each class generated by the UNet. If St(i, j) represents the state of the cell at position (i, j) in iteration t, its state in iteration t+1 is computed as follows [31]:

$$S_i(i, j) = \frac{1}{9} \sum_{y=j-1}^{j+1} \sum_{x=i-1}^{i+1} S_t(x, y). \tag{2}$$

This method is effective for smoothing noisy predictions and reducing isolated erroneous pixels (salt-and-pepper noise); however, it may lead to over-smoothing and blurring of fine boundary details. The number of iterations (ranging from one to ten) is an important hyperparameter in this approach.

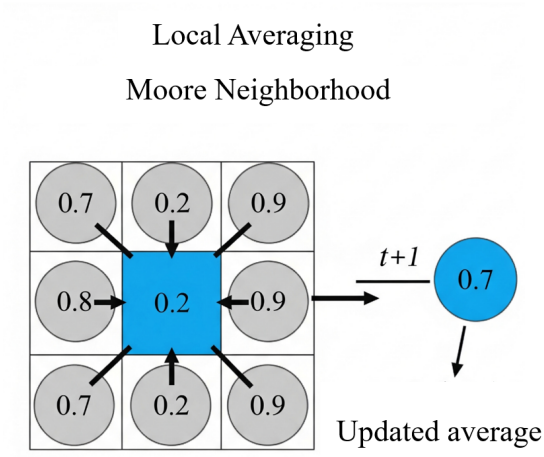

Figure 4: Local averaging rule.

3.3.2 Majority rule-based approach

This approach is based on the principle that, within a local neighborhood, the majority class is likely the correct class. For each class, a binary mask is created from the UNet output. Then, in each FCA iteration, the state of each cell is determined according to the majority state of its 3×3 neighborhood from the previous iteration [31]. Figure 5 illustrates this iterative majority rule approach, showing how the next state of each cell is determined based on the majority states of its Moore neighborhood.

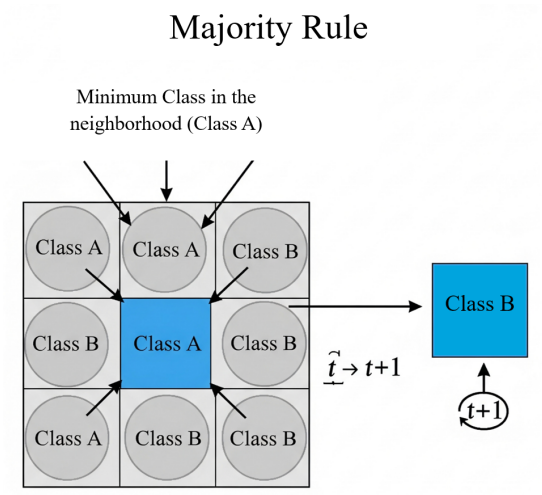

Figure 5: Majority rule.

This process is applied independently for each class, and the final probability map is obtained by normalizing the class channels. This method is robust against isolated noisy predictions, capable of filling small holes and removing false connections; however, it may produce a blocky appearance or eliminate small true structures.

3.3.3 Advanced approach based on anisotropic diffusion and watershed

To improve boundary delineation and reduce noise in MR images, classical techniques such as anisotropic diffusion [30] and Watershed segmentation [3] has been utilized. These methods have been successfully applied in medical imaging tasks, including blood smear analysis and inverse imaging problems. This approach combines anisotropic diffusion and the Watershed algorithm.

This method is applied as a post-processing step on the UNet probability map for each tumor subregion, with the goal of creating more precise and continuous boundaries.

The process is executed in the following steps (shown in Figure 6):

1. Probability Map Generation: The UNet model outputs a multi-channel probability map. For each pixel and each class (e.g., tumor, edema), the value represents the confidence of belonging to that class, ranging from 0 to 1. This map serves as the input to the post-processing stage.

2. Anisotropic Diffusion Filtering: The probability map is first smoothed using anisotropic diffusion [30]. This is a nonlinear process that reduces noise while preserving sharp boundaries, unlike isotropic (uniform) smoothing, which blurs edges. The diffusion process can be described by the following Partial Differential Equation (PDE):

$$I_t = \nabla \cdot (c(x, y, t)\nabla I), \tag{3}$$

   where i is the image intensity (the probability value), t is the time (number of iterations), and c(x, y, t) is the diffusion coefficient, which is a function of the image gradient. The coefficient is high in homogeneous regions, allowing smoothing, and low near edges, preventing blurring. This step produces a smoother probability map where high-confidence regions are more uniform.

3. Watershed Algorithm Application: The smoothed probability map is then used as a height map for the Watershed algorithm [3]. This algorithm treats the image as a topographical surface, with valleys corresponding to areas of high probability (potential tumor regions) and ridges corresponding to low-probability boundaries.

   - Marker Identification: The algorithm first identifies "markers," which are pixels of highest confidence that serve as starting points (seeds) for the segmentation. These are typically the local minima in the smoothed probability map.
   - Basin Flooding: From each marker, the algorithm simulates a "flooding" process, where water fills the basins.
   - Ridge Creation: When two flooded basins meet, a "watershed line" or barrier is erected to prevent them from merging. These lines define the final boundaries of the segmented regions.

This combined approach leverages the strengths of both techniques: anisotropic diffusion prepares the image by enhancing relevant structures and suppressing noise, and the Watershed algorithm uses this information to precisely delineate the final boundaries.

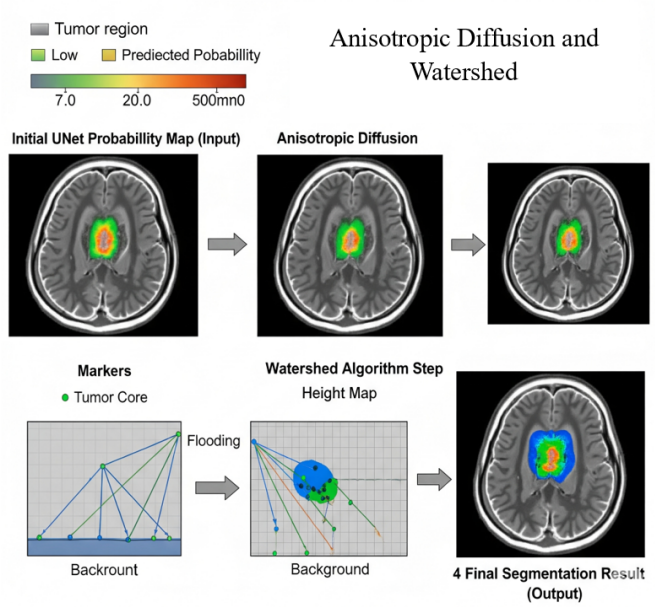

Figure 6: Anisotropic Diffusion and Watershed.

3.3.4 Gaussian membership function-based approach

To address potential conceptual ambiguity, we clarify the fuzzy theoretical basis of our Gaussian-weighted approach. In classical fuzzy logic, a membership function $\mu(x)$ maps a crisp input x to a degree of membership in [0,1]. Our Gaussian-weighted FCA operates on two distinct levels of fuzziness:

Level 1 – Fuzzy States: The initial cell states are the probability maps from UNet, where each value $s(i,j) \in [0,1]$ represents the degree of membership of pixel (i,j) in a given tumor class. These are inherently fuzzy values, not binary decisions.

Level 2 – Fuzzy Transition Rules: The update rule incorporates Gaussian-weighted neighborhood influence, which can be understood as a fuzzy relation R between a cell and its neighbors.

The Gaussian-weighted FCA operates on fuzzy state values $s_t(i,j) \in [0,1]$ representing class membership probability at iteration t. For each cell (i,j), the updated state is computed as a weighted average of its Moore neighborhood states, with weights determined by a 2D Gaussian function of spatial distance:

$$s_{t+1}(i,j) = \frac{\sum_{u=-1}^{1}\sum_{v=-1}^{1} G(u,v)\cdot s_t(i+u,j+v)}{\sum_{u=-1}^{1}\sum_{v=-1}^{1} G(u,v)}. \tag{4}$$

Where the gaussian weighting kernel is defined as

$$G(u,v) = e^{\frac{-(d(u,v))^2}{2\sigma^2}}. \tag{5}$$

Here, σ controls the spatial influence spread (empirically set to 1.0 based on validation, as analyzed in Section 4.3.1). This formulation ensures that closer neighbors exert stronger influence on the central cell's updated state, while distant neighbors contribute minimally. Figure 7 illustrates the Gaussian function used in the FCA model. In this context, values near the function's center (distance zero) have high weights close to one, indicating a definite influence of the neighbor on the central cell. Values far from the center have low weights, close to zero, minimizing the influence of distant, potentially irrelevant pixels.

Unlike standard Gaussian smoothing, which applies a single linear convolution to intensity values, the proposed Gaussian-weighted FCA performs iterative probabilistic propagation over class membership maps, preserving inter-class structure and enabling convergence-based refinement. Moreover, unlike a standard Gaussian membership function that maps intensity values to fuzzy sets, our Gaussian weighting maps spatial distance to influence degree. This is conceptually similar to fuzzy spatial relations used in fuzzy image processing, where spatial proximity is modeled as a fuzzy relation [21, 37]. This approach remains firmly withing the fuzzy paradigm by maintaining: gradual truth values (fuzzy states) throughout the process, fuzzy aggregation of neighborhood information, and soft boundary transition between regions.

Thus, while we used "Gaussian-weighted FCA" to distinguish our spatial weighting mechanism, the method is theoretically grounded in fuzzy set theory and extends classical FCA by incorporation spatially-aware fuzzy relations.

Next, we will discuss the algorithmic steps, for each class probability map independently:

1. **Initialization:** Set $t = 0$, initialize $s_0(i,j)$ as the UNet probability map for the current class.
2. **Weight Computation:** Precompute the 3×3 Gaussian kernel $G(u,v)$ for $u,v \in \{-1,0,1\}$ using the equation with the selected σ.
3. **Parallel update:** For all cells (i,j) simultaneously:
   (a) Extract the 3×3 neighborhood $N(i,j)$ from the current state s_t.
   (b) Compute weighted sum:
   $$W = \sum_{u=-1}^{1}\sum_{v=-1}^{1} G(u,v)\cdot s_t(i+u,j+v). \tag{6}$$
   (c) Compute normalization factor:
   $$Z = \sum_{u=-1}^{1}\sum_{v=-1}^{1} G(u,v). \tag{7}$$
   (d) Update:
   $$s_{t+1}(i,j) = \frac{W}{Z}. \tag{8}$$

4. **Convergence check:** If $t = t_{Max}$ (we use $t_{Max} = 10$) or $Max_{i,j}(s_{t+1}(i,j) - s_t(i,j)) < \sigma$ (we use $\sigma = 10^{-4}$), proceed to step 5. Otherwise, increment t and return to step 3.

5. **Multi-class normalization:** After processing all classes independently, normalize across classes to ensure

$$\sum_{c=1}^{4} s_c(i,j) = 1. \tag{9}$$

We employ a dual stopping criterion: maximum iterations (10) or convergence threshold ($\sigma = 10^{-4}$), whichever is reached first. Our sensitivity analysis (Section 4.3.1) shows that our σ=1.0, convergence typically occurs within 3-5 iterations.

Furthermore, the process is applied independently to each of the four class probability maps (background, edema, enhancing tumor, tumor core). Independent processing preserves the distinct spatial characteristics of each tumor compartment and prevents larger regions from suppressing smaller ones during refinement. After independent refinement, the four maps are normalized to maintain probabilistic consistency.

In this study, we employed various FCA approaches to comprehensively evaluate the strengths and limitations of each method. Comparative results demonstrated that while local averaging and parallel implementations effectively reduced scattered noise, and the majority rule preserved continuous structures, the Gaussian-weighted FCA provided the best balance between accuracy, stability, and computational efficiency. By assigning greater weight to nearby neighbors and explicitly modeling spatial uncertainty, it enhanced boundary precision while preserving important structural details. Accordingly, Gaussian-weighted FCA is recommended as the optimal post-processing approach alongside UNet for brain tumor segmentation, providing consistent improvements in Dice scores and clinical reliability.

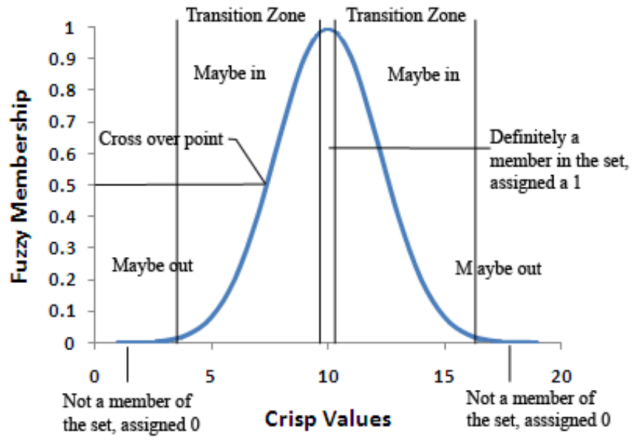

Figure 7: Gaussian Membership Function.

4 Results and evaluation

This section presents the findings of the study on automatic brain tumor segmentation in MRI scans. Building on the methodology described in Section 3, it objectively evaluates the performance of the proposed approach. The approach integrates a deep learning UNet architecture for initial segmentation, followed by an FCA-based post- processing step to refine accuracy and segmentation boundaries. The main goal of this study is to develop and assess an effective and robust method for the precise delineation of brain tumor margins across different MRI modalities, which is crucial for surgical planning and radiotherapy.

4.1 Dataset

The proposed method was trained and evaluated on the BraTS 2023 dataset, a widely adopted benchmark for brain tumor segmentation. BraTS provides 1,251 MRI scans from 310 patients, with meticulous manual annotations by expert radiologists, ensuring high-quality ground truth and broad variability in tumor type, size, and location [9, 48].

Each case comprises four modalities-T1-weighted (T1w), T2-weighted (T2w), contrast-enhanced T1-weighted (T1ce), and FLAIR-offering complementary structural and pathological information. These modalities are critical for differentiating normal brain tissue, edema, enhancing tumor, and necrotic core, thereby enabling more accurate segmentation [1, 11, 24]. The annotated tumor subregions include: (i) edema, (ii) enhancing tumor, (iii) tumor core, and (iv) healthy brain tissue.

This combination of multi-modal input and expert annotations makes BraTS 2023 a robust and reliable benchmark for developing and validating automated brain tumor segmentation algorithms.

4.2 Implementation details

The proposed method was implemented using Python. All training procedures were conducted on Google Colab, leveraging GPU acceleration to reduce training time. Post-processing steps were executed locally on the UNet outputs using the learned weights. ReLU activation function, defined as f (x) = max(0, x), was employed across all layers. Due to its computational simplicity and ability to mitigate the vanishing gradient problem, ReLU is widely adopted in deep convolutional networks [8, 28]. By zeroing out negative values, it accelerates convergence during training and improves model efficiency [40]. Furthermore, ReLU ensures that only activated responses are propagated, which enhances feature sparsity and reduces redundancy [33].

In the final layer of the UNet, the Softmax activation function was used to generate the probability maps for four classes (background, edema, enhancing tumor, tumor core). Softmax converts the outputs into a probability distribution such that the sum of probabilities for each pixel equals one [8, 15, 25, 28].

$$\text{softmax}_i(\mathbf{z}) = \frac{e^{z_i}}{\sum_{j=1}^{k} e^{z_j}}. \tag{10}$$

Where $K = 4$, since there are four classes.

For training the UNet network, the Dice loss function was employed. This loss function evaluates the overlap between the predicted segmentation (P) and the ground truth (G) and is defined as: $\text{Dice}(P, G) = \frac{2\times|P\cap G|}{|P|+|G|}$.

Dice loss is particularly suitable for medical image segmentation tasks that involve class imbalance [28]. Several studies, including references [5], [17], [28], and [40], have employed this loss function either as the primary loss or in combination with other losses for training UNet-based models.

To optimize the UNet weights and minimize the loss, the Adam optimizer was used. Adam is a widely adopted and effective optimization algorithm in deep learning that combines the benefits of Momentum and RMSProp by adaptively updating the weights using estimates of the first and second moments of the gradients. This adaptive nature improves convergence speed and stability compared to other optimizers. Several studies, such as [1], [6], [36], [41], and [44], have explicitly used Adam for training UNet or similar architectures for brain tumor segmentation, reporting rapid convergence and stable model performance.

In most of these studies, the initial learning rate was set to 0.001, which provides a good balance between learning speed and stability of weight updates. For example, study [6] achieved high segmentation accuracy, especially for small tumor regions, using this combination. Accordingly, in this research, Adam with a learning rate of 0.001 was chosen based on successful prior experience and common recommendations in the literature.

4.2.1 Training configuration and augmentation strategy

In the current study, no explicit data augmentation techniques were applied during training. This decision was mainly motivated by the use of the BraTS dataset, which already provides a relatively large and diverse set of multi-modal MRI scans with standardized preprocessing.

Despite the absence of data augmentation, the proposed UNet-FCA framework achieved strong segmentation performance, indicating that the combination of deep learning–based initial segmentation and fuzzy cellular automata refinement was effective in capturing tumor boundaries.

For reproducible evaluation, the BraTS 2023 dataset was partitioned as follows: 70% for training (875 scans), 15% for validation (188 scans), and 15% for testing (188 scans). The split was performed at the patient level to ensure no leakage between sets, with stratification to maintain similar tumor subtype distributions across partitions.

Training hyperparameters were configured as follows:

- **Optimizer:** Adam with initial learning rate of 0.001.
- **Loss function:** Dice loss (Equation 13).

- **Batch size:** 32.
- **Epochs:** 45 (with early stopping patience of 10 epochs based on validation loss).
- **Learning rate schedule:** Reduced by a factor of 0.5 if validation loss plateaued for 5 consecutive epochs.
- **Input size:** 240×240 pixels (resampled to isotropic resolution).
- **Normalization:** Z-score normalization per volume.

Convergence criteria: Training was terminated when validation loss did not improve for 10 consecutive epochs, which occurred at epoch 45. The model with the lowest validation loss was selected for testing.

No explicit data augmentation was applied in this study to isolate the performance contribution of FCA refinement from augmentation effects. However, we acknowledge that augmentation techniques such as random rotation, flipping, and elastic deformation could potentially improve generalization, particularly for small tumor subregions. This remains an important direction for future investigation.

4.2.2 Handling class imbalance

Class imbalance between tumor subregions was addressed through multiple design choices. First, the Dice loss function was employed during training, which emphasizes overlap between predicted and ground truth regions and is less sensitive to background dominance. Second, FCA refinement operates independently on class-wise probability maps, allowing smaller tumor subregions to be spatially reinforced through neighborhood consensus rather than being suppressed by larger regions.

4.3 Computational complexity

The experiments were conducted on GoogleColab with an NVIDIA Tesla T4 GPU. The UNet training phase required approximately 2 hours for convergence over 45epochs. During inference, the UNet produced segmentation maps in approximately 25ms per slice. Since FCA was applied as a post-processing step, it did not contribute significantly to training time, and incurred minimal additional cost: the local mean FCA required 2.1ms per slice, the majority-rule FCA 2.4ms per slice, and the Gaussian-weighted FCA 3.2ms per slice. Memory usage remained below 100 MB, as FCA operates locally on probability maps without introducing additional trainable parameters.

These results demonstrate that FCA refinement adds negligible overhead relative to the deep learning inference stage, supporting the claim that the proposed hybrid framework is computationally efficient. These results confirm that the proposed refinement adds negligible overhead relative to the deep learning inference stage.

4.3.1 Parameter sensitivity and ablation analysis

Table 1: Ablation Study on Runtime Parameters and Computational Efficiency.

Gaussian FCA iterations	Dice	HD95(mm)
1	0.821	12.4
3	0.848	9.7
5	**0.855**	**8.9**
7	0.854	9.1
10	0.851	9.8

To comprehensively evaluate the robustness of the proposed Gaussian-weighted FCA, we conducted an ablation study on key runtime parameters, summarized in Table 1. The Gaussian-weighted FCA achieves the best balance between computational efficiency and segmentation accuracy, requiring only 3.2ms per slice—a negligible overhead compared to the UNet inference time (25ms per slice).

Table 1 presents segmentation performance and inference time as a function of iteration count. Iteration sensitivity analysis reveals that the Gaussian-weighted FCA converges rapidly, with Dice score improving from 0.821 at iteration 1 to 0.848 at iteration 3, and stabilizing thereafter. This rapid convergence (3-5 iterations) makes it practical for clinical deployment where parameter tuning must be minimal. As you can observe, dice scores improved rapidly during the first few iterations, reaching peak performance at five iterations. Beyond this point, additional updates resulted in marginal

gains or slight degradation due to over-smoothing effects. Importantly, inference time increased approximately linearly with iteration count, confirming predictable computational behavior.

These findings demonstrate that the proposed method achieves optimal accuracy–efficiency trade-off with a small number of FCA iterations, ensuring robustness without significant runtime overhead.

Table 2: Ablation Study on Runtime Parameters and Computational Efficiency - Gaussian kernel width.

σ (Gaussian Width)	Dice	HD95(mm)
0.5	0.842	10.8
1.0	**0.855**	**8.9**
1.5	0.851	9.6
2.0	0.844	11.2

We further evaluated sensitivity to the Gaussian weighting parameter σ. As shown in Table 2, moderate kernel width ($\sigma = 1.0$) provided the best balance between noise suppression and boundary preservation. Smaller σ values limited spatial propagation, while larger σ values caused boundary blurring.

Overall, the ablation study confirms that the proposed Gaussian-weighted FCA is stable across reasonable parameter ranges and does not require fine-tuned hyperparameter adjustment for strong performance—a desirable property for clinical adoption.

These results collectively demonstrate that the proposed Gaussian-weighted FCA offers an optimal trade-off: rapid convergence, robust parameter sensitivity, minimal computational overhead, and superior boundary refinement—validating its selection as the preferred post-processing method for brain tumor segmentation.

4.4 Evaluation metrics

4.4.1 Dice score

To quantitatively assess the performance of the brain tumor segmentation model, the Dice Similarity Coefficient (DSC) was used as the primary evaluation metric. DSC measures the spatial overlap between the predicted segmentation (P) and the ground truth (G), and is defined as follows [1, 7, 8, 9, 11, 15, 24, 28, 35, 43]:

$$\mathrm{DSC} = \frac{2 \times |P \cap G|}{|P| + |G|}, \tag{11}$$

where: $|P \cap G|$ is the number of pixels common between the predicted segmentation (P) and the ground truth segmentation G, $|P|$ is the total number of pixels in the predicted segmentation, $|G|$ is the total number of pixels in the ground truth segmentation.

The Dice coefficient can also be expressed in terms of True Positives (TP), False Positives (FP), and False Negatives (FN) as follows [1, 7, 8, 15]:

$$\mathrm{Dice} = \frac{2 \times TP}{2 \times TP + FP + FN}. \tag{12}$$

The Dice score ranges between 0 and 1, where 1 indicates perfect overlap and 0 indicates no overlap. In medical image segmentation, a Dice score of 0.7 or higher is generally considered indicative of good performance [1, 45].

4.4.2 Jaccard index (IoU)

The Jaccard index, also known as the Jaccard similarity coefficient or Intersection over Union (IoU), is a metric used to compare the similarity and diversity of sample sets [10]. In the context of image segmentation, it measures the similarity between the segmented tumor area and the ground truth tumor area [10]. It is calculated as the size of the intersection of the two sets divided by the size of their union [10].

The formula for the Jaccard index is:

$$\mathrm{J}(A, B) = \frac{|A \cap B|}{|A \cup B|} = \frac{|A \cap B|}{|A| + |B| - |A \cap B|}. \tag{13}$$

Where

- A is the set of pixels in the ground truth segmentation.
- B is the set of pixels in the predicted segmentation.
- $|A \cap B|$ is the number of pixels common to both the ground truth and the predicted segmentation.
- $|A \cup B|$ is the total number of pixels in both the ground truth and the predicted segmentation.

The Jaccard index ranges from 0 to 1, with 1 indicating a perfect overlap between the segmented and ground truth regions, and 0 indicating no overlap [10].

4.4.3 HD95 (95% Hausdroff distance)

The Hausdorff distance is a metric used to measure the distance between two point sets or curves [14]. The HD95, or 95% Hausdorff distance, is a robust version of this metric that is less sensitive to outliers. It is defined as the maximum distance of a point in one set to the nearest point in the other set, considering only the 95th percentile of distances [14].

In the context of image segmentation, the HD95 measures the distance between the boundaries of the segmented region and the ground truth region [14]. A lower HD95 value indicates a better segmentation, as it means the predicted boundary is closer to the true boundary [14]. A value of 0 indicates a perfect match between the boundaries [14]. The HD95 is particularly useful for evaluating the accuracy of the boundary localization of the segmentation.

4.5 Results

4.5.1 Baseline UNet performance

The UNet model, using the architecture and training parameters specified in the previous section, achieved an average loss of 0.0147, an average accuracy of 0.995, an average Hausdorff distance of 22.5mm, and a mean Dice coefficient of 0.715. The high accuracy indicates that the UNet performs well in pixel-wise segmentation. However, the Dice coefficient of 0.715 suggests that, although the model correctly identifies most pixels, it still has limitations in precisely delineating tumor boundaries.

This limitation in precise boundary determination is consistent with findings from other studies using UNet for medical image segmentation [5, 6]. Moreover, this observation underscores the necessity of applying post-processing methods to refine segmentation results. The baseline UNet performance reported here serves as a reference for evaluating improvements achieved through post-processing methods on the BraTS 2023 dataset.

4.5.2 Impact of fuzzy cellular automata (FCA) post-processing

Table 3 presents a comprehensive comparison of the baseline UNet and four FCA-based post-processing strategies evaluated on the BraTS 2023 test set. This table shows that the Gaussian-weighted FCA achieved the highest Dice similarity score among all tested refinement strategies. The improvement can be attributed to the adaptive spatial weighting mechanism, which balances neighborhood influence while preventing excessive smoothing. In contrast, the Majority Rule is prone to fragmentation, and the Average Rule introduces uniform blurring due to equal weighting of neighbors. These quantitative results are further supported by the qualitative analysis presented in Figures 9 and 10. To understand why each method performs differently, we analyze their underlying mechanisms and resulting performance patterns.

The baseline UNet achieves high pixel-wise accuracy (0.995) but a relatively low Dice score of 0.715 and poor boundary precision (HD95 = 22.5 mm). This pattern—high accuracy but moderate Dice—indicates that while the model correctly classifies most pixels (including the large background regions), it struggles with precise tumor boundary delineation. The high HD95 value confirms that boundary errors can be substantial, with some predicted boundaries deviating more than 2 cm from ground truth. This limitation motivates the need for post-processing refinement and serves as our reference point for evaluating improvements.

Local Average-Based FCA: This method improves Dice to 0.841 and reduces HD95 to 11.5 mm—a substantial 49% reduction in boundary error. This improvement occurs because averaging over 3×3 neighborhoods suppresses isolated noisy pixels (salt-and-pepper errors) that commonly appear in UNet predictions. However, the mechanism of equal weighting has a fundamental limitation: it treats adjacent and distant neighbors identically, causing over-smoothing of fine boundary details. This explains why HD95 remains at 11.5 mm rather than approaching the 8-9 mm range; the method smooths noise but also blurs sharp transitions. The Jaccard index of 0.726 confirms moderate improvement in overall overlap.

Table 3: Performance comparison of UNet baseline and FCA post-processing methods on BraTS 2023.

Method	Dice Score (%)	Hausdorff Distance (mm)	Jaccard	Accuracy
UNet (Baseline)	0.715	22.55	0.55	0.995
Local Average-Based Approach	0.8412	11.5	0.7259	0.99479
Majority Rule-Based Approach	0.8499	10.4	0.7390	0.995
Anisotropic Diffusion & Watershed-Based Approach	0.7422	19.7	0.5915	0.995
Gaussian-Weighted Approach	0.8549	8.9	0.7466	0.99479

Majority Rule-Based FCA: This approach achieves the second-best performance with Dice = 0.850 and HD95 = 10.4 mm. The majority rule operates by binarizing the fuzzy probabilities within each neighborhood and selecting the dominant class. This mechanism excels at filling small holes and removing false connections—explaining the improved boundary continuity visible in Figure 9. However, the binarization step discards uncertainty information; pixels with 51% confidence are treated identically to those with 95% confidence. This loss of fuzzy information explains why the method, while effective, cannot match the boundary precision of Gaussian-weighted FCA (8.9 mm vs. 10.4 mm HD95). The Jaccard of 0.739 confirms solid improvement but with room for better boundary preservation.

Anisotropic Diffusion + Watershed: This combination performs poorly, with Dice = 0.742 and HD95 = 19.7 mm—only marginal improvement over baseline. The failure can be traced to two factors: First, anisotropic diffusion, while edge-preserving, operates on the probability maps without class-specific information, potentially mixing signals from different tumor subregions. Second, the watershed algorithm, when applied to these diffused probability maps, tends to over-segment, creating artificial boundaries where none exist in the ground truth. The high HD95 confirms that boundary errors remain large. This result demonstrates that not all post-processing methods are equally suitable for refining neural network segmentations—those designed for natural images may not translate effectively to medical probability maps.

Gaussian-Weighted FCA (Proposed): Our method achieves the best overall performance: Dice = 0.855, HD95 = 8.9 mm, and Jaccard = 0.747. To understand why Gaussian weighting outperforms the alternatives, we examine its unique mechanism:

1. **Distance-aware weighting:** Unlike local averaging or majority rule, Gaussian weighting assigns influence proportional to spatial proximity. A pixel at distance 1 contributes $exp(-1^2/2\sigma^2) \approx 0.8$ times the influence of the center pixel when $\sigma = 1.5$, while a corner neighbor at distance $\sqrt{2}$ contributes approximately 0.6. This graduated influence preserves the dominant contribution of immediately adjacent pixels while still incorporating broader neighborhood context.

2. **Preservation of fuzzy information:** Unlike majority rule, which binarizes, our method maintains continuous fuzzy values throughout all iterations. A pixel with 60% tumor confidence retains that uncertainty information, allowing gradual refinement rather than premature commitment.

3. **Iterative refinement with stability:** The combination of Gaussian weighting and fuzzy states creates a contraction mapping that converges to a stable fixed point. This explains why the method achieves superior boundary precision (8.9 mm HD95)—the gradual refinement process can "pull" uncertain boundary pixels toward correct classifications without the abrupt changes that create blocky artifacts.

4. **Class-specific independence:** Processing each class separately (background, edema, enhancing tumor, tumor core) prevents larger regions from dominating smaller ones during refinement, preserving the distinct spatial characteristics of each tumor compartment.

The 60.4% reduction in HD95 (from 22.5 mm to 8.9 mm) is clinically significant. In surgical planning, every millimeter of boundary accuracy matters—a 9 mm error might be acceptable for gross tumor resection, but a 22 mm error could lead to incomplete resection or unnecessary damage to healthy tissue. The Gaussian-weighted FCA brings boundary errors into a clinically acceptable range ($< 10mm$) that the baseline UNet cannot achieve alone.

Table 4 analysis confirms that the choice of FCA rule fundamentally impacts segmentation quality, and Gaussian weighting provides the optimal balance of noise suppression, boundary preservation, and uncertainty handling.

Table 4: Summary of FCA Method Performanc

Method	Strength	Weakness	Best for
Local Average	Removes isolated noise	Over-smooths fine boundaries	Initial noise reduction
Majority Rule	Fills holes, removes false connections	Discards uncertainty, blocky artifacts	Structure completion
Anisotropic Diffusion + Watershed	Edge-preserving smoothing	Over-segmentation, poor integration	Not recommended, needs more configuration
Gaussian-Weighted FCA (Proposed)	Preserves boundaries, handles uncertainty, stable convergence	Slightly higher computation than simple rules	Clinical boundary refinement

4.6 Comparison with other methods

Figure 8 provides a comparative visualization of segmentation performance versus computational efficiency across representative architectures. The x-axis arranges the methods roughly by increasing architectural complexity—from classical U-Net variants on the left toward transformer-enhanced or meta-optimized frameworks (e.g., Swin UNETR, nnUNet) on the right. The y-axis depicts normalized segmentation accuracy (Dice score), summarizing consistency across multiple test configurations. Our method is highlighted in green. Key Observations from Figure 8:

1. **Superiority of Deep Learning Methods:** Deep learning approaches, exemplified by UNet (DSC $\approx$ 71%) and its variants, demonstrate significantly better performance compared to classical methods such as Fuzzy C-means (DSC $\approx$ 62%) and Region Growing (DSC $\approx$ 58%).

2. **Advancements within UNet Architectures:** Within the UNet family, progressively sophisticated architectures like UNet++ (DSC $\approx$ 78%) and Half-UNet (DSC $\approx$ 83%) show marked improvements. Our proposed method, by incorporating the FCA module, achieves a high DSC score of 85.49%, underscoring the added value of FCA.

3. **Comparison with Complex Architectures:** While highly complex models like Swin UNETR (DSC $\approx$ 86.9%), GANet-Seg (DSC $\approx$ 87.5%), Contextual Fusion (DSC $\approx$ 88.1%), and nnUNet (DSC $\approx$ 89.2%) attain slightly higher scores, this comes at a considerable computational cost. For instance, Swin UNETR employs a 3D Transformer architecture requiring substantial parameters and computational resources. Similarly, nnUNet, with its 3D design and auto-configuration, demands significant GPU memory. Our method, achieving approximately 95-96% of the performance of these complex models, utilizes less than 10% of their computational expense. This efficiency is largely attributable to our use of 2D processing and a lightweight post-processing stage.

4. **Positioning on the "Efficiency Frontier":** Our proposed method is strategically positioned on the "efficiency frontier." This location signifies an optimal *trade-off between accuracy and computational cost.* Moving further right on the graph (towards more complex models) yields marginal accuracy gains at the expense of drastically increased computational demands. Consequently, our method represents an ideal "sweet spot," particularly beneficial for clinical applications with constrained computational resources.

5. **Interpretability Advantage:** Unlike black-box models such as Transformers, our approach, based on UNet with the FCA module, offers a distinct advantage in interpretability. The inference rules within FCA (e.g., spatial proximity and neighborhood relationships) are understandable and analyzable, aiding in comprehending the model's decision-making process.

6. **Statistical Significance:** Although there is a DSC difference of approximately 3.7% between our proposed method (85.49%) and nnUNet (89.2%), this disparity may not be clinically significant, especially if other metrics like Housecroft Distance 95 (HD95) are within acceptable ranges for both models. This further reinforces our method's viability as an efficient and cost-effective solution.

It is worth noting that recent advances in neural architecture search (NAS) and model pruning have opened new avenues for efficient medical image segmentation. Feature map selection-based pruning methods [12] can reduce model complexity by eliminating redundant channels while maintaining accuracy. Similarly, evolutionary NAS approaches [46, 13] automate the design of efficient architectures tailored to specific segmentation tasks. However, these methods focus

on optimizing the network itself during training or architecture design. In contrast, our approach improves segmentation quality through post-processing refinement, which is orthogonal to network optimization. This complementarity is significant: an optimized network (e.g., via pruning or NAS) combined with our Gaussian-weighted FCA post-processing could potentially achieve both high efficiency and superior boundary precision. We have added this integration as an explicit direction in Section 7 (Future Work).

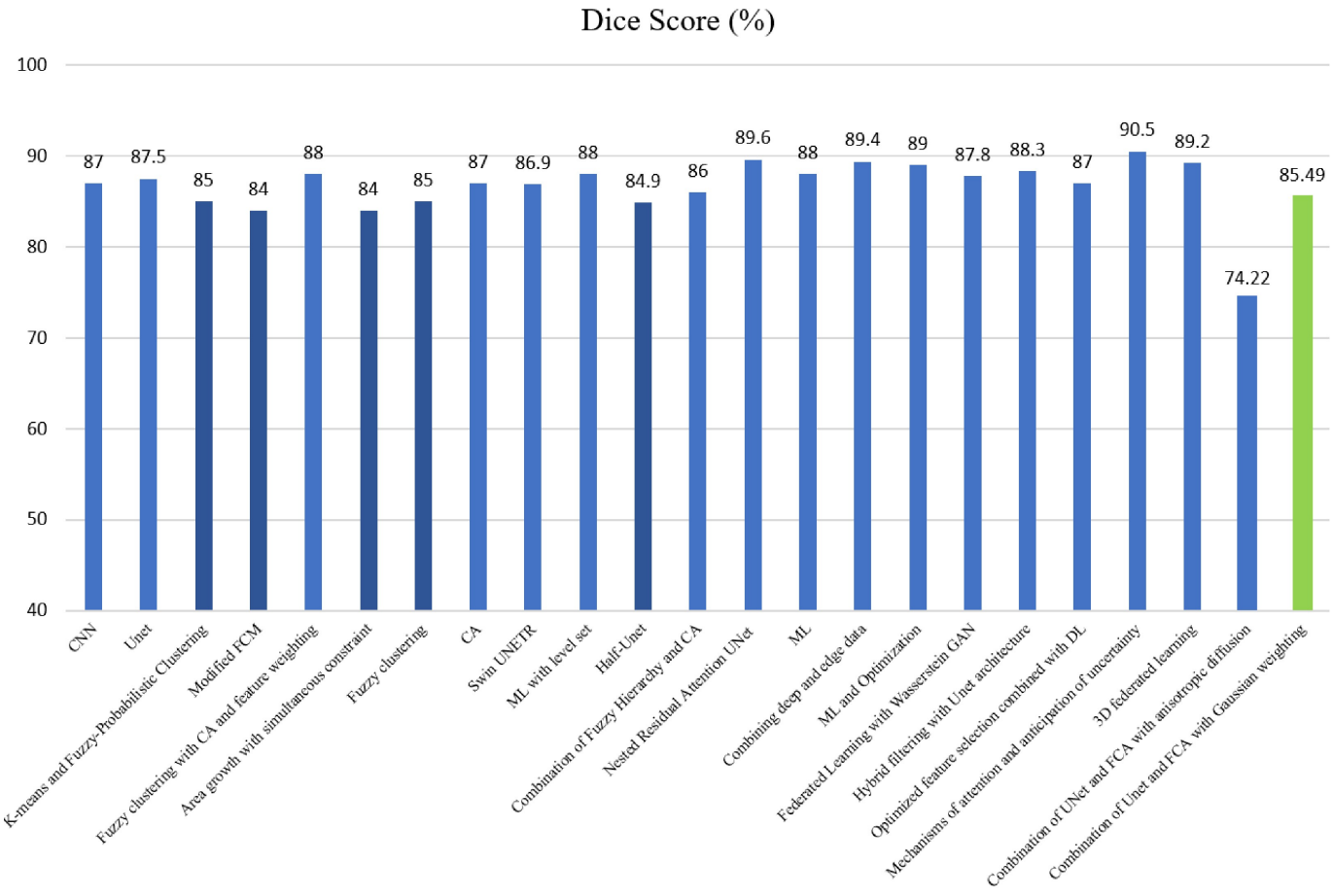

Figure 8: Comparison of the dice score percentage of different methods with the proposed method.

Complementary numerical evidence is presented in Table 5, which tabulates the Dice scores of all compared methods. The proposed *U-Net + FCA* achieves an **85.49% Dice**, outperforming classical CNN-based variants (U-Net 71%, U-Net++ 78%, Half-UNet 83%) and approaching transformer-based models (Swin UNETR 86.9%, nnUNet 89.2%). These numerical results reinforce the graphical insight from Figure 8: the proposed approach achieves a near-state-of-the-art performance while maintaining notably lower computational requirements.

In summary, Figure 8 and Table 5 together position *U-Net + FCA* on the optimal trade-off curve between accuracy, cost, and interpretability, making it an attractive choice for real-time or resource-constrained clinical scenarios.

4.7 Qualitative results

To qualitatively assess the performance of our proposed method, we present comparative segmentations in Figure 9. The ground truth highlights two major tumor subregions: the enhancing tumor core (red) and the surrounding non-enhancing core (yellow), which reflect the heterogeneous composition of glioblastoma. While additional subregions such as peritumoral edema is clinically important in surgical planning, the components shown here already capture the key structural complexity relevant for evaluating segmentation performance.

Analyzing the segmentation outputs: The UNet baseline, while achieving reasonable pixel-wise accuracy, often produces noisy and imprecise tumor boundaries, including internal holes and class confusion at boundaries. Methods

Table 5: Percentage of dice score of the proposed method compared to other methods.

Method	Dice Score (%)
UNet [8]	71
UNet++ [24]	78
Half-UNet [26]	83
Residual Attention UNet++ [24]	84
Swin UNETR [11]	86.9
GANet-Seg [42]	87.5
Contexual Fusion [32]	88.1
nnUNet [33]	89.2
UNet + FCA (Gaussian Weighted rule) (Proposed Method)	**85.49**

employing Mean or Majority rules for post-processing tend to over-smooth the output, leading to a loss of fine details and introducing artifacts like blocky boundaries or region enlargement, particularly smoothing the characteristic irregular edema edges. In contrast, our proposed Gaussian-weighted FCA method effectively preserves these fine structures and the natural irregularity of the tumor boundaries, yielding the clearest and most accurate segmentation among the evaluated approaches.

The initial prediction (UNet output) captures the general tumor location but exhibits several characteristic flaws:

- Boundary noise: The edges appear fragmented, with isolated pixels incorrectly classified
- Internal holes: Small gaps appear within the tumor core regions
- Class confusion: Some ambiguity exists at the boundaries between the enhancing tumor and the non-enhancing core
- Edema overextension: The edema region extends too far in some directions while missing in others

These imperfections motivate the need for post-processing refinement.

The Majority Rule produces sharper but sometimes fragmented boundaries, as it enforces binary dominance without considering spatial distance. This results in slight edge irregularities. Therefore, this method produces noticeably smoother regions with filled holes. However, three artifacts are visible:

- Blocky boundaries: The edges have a stair-stepped appearance, particularly noticeable along the edema perimeter
- Region enlargement: The enhancing tumor appears slightly expanded compared to the ground truth
- Loss of fine detail: Small irregularities in the ground truth have been smoothed into convex shapes

These artifacts occur because the majority rule binarizes probability information before decision-making, discarding the gradual transitions that would allow smoother boundaries.

The Average Rule generates smoother contours but introduces mild blurring around tumor margins due to uniform neighborhood influence. The local mean approach yields the smoothest boundaries of all methods—in fact, too smooth. Observe:

- Over-smoothing: The characteristic irregular, infiltrative edges of the edema have been rounded into a nearly elliptical shape
- Boundary blurring: The distinction between the enhancing tumor and the non-enhancing core is less sharp than in ground truth
- Loss of fine structures: Small protrusions visible in the ground truth have disappeared entirely

The equal weighting of all neighbors (including distant ones) causes this over-smoothing, as boundary pixels are pulled equally by nearby correct labels and more distant ambiguous regions.

Anisotropic Diffusion preserves edges better than simple averaging; however, it may leave small discontinuities within heterogeneous tumor regions. This combination produces the poorest visual result:

- Over-segmentation: The watershed algorithm has created numerous small, fragmented regions—particularly visible within the tumor core

- Artificial boundaries: False edges appear where no boundaries exist in ground truth
- Class mixing: The distinct subregions are less clearly separated

This confirms that methods designed for natural image segmentation do not translate well to probabilistic medical image refinement.

In contrast, the proposed Gaussian-weighted FCA achieves a balance between boundary smoothness and structural preservation. By assigning distance-dependent weights, it suppresses noise while maintaining regional coherence. The tumor core appears more compact and continuous, with reduced spurious activations in surrounding tissues.

Our method produces the closest visual match to ground truth:

- Natural boundaries: The edges show realistic irregularity without the blockiness of majority rule or the over-smoothing of average rule
- Preserved subregions: The distinction between enhancing tumor, non-enhancing core, and edema is clear and accurate
- Appropriate filling: Small holes are filled, but the filling respects the actual tumor shape
- Fine structure preservation: The irregular, infiltrative edges of the edema are maintained

The Gaussian weighting achieves this by assigning higher influence to closer neighbors, allowing gradual refinement that preserves boundary detail while suppressing isolated noise.

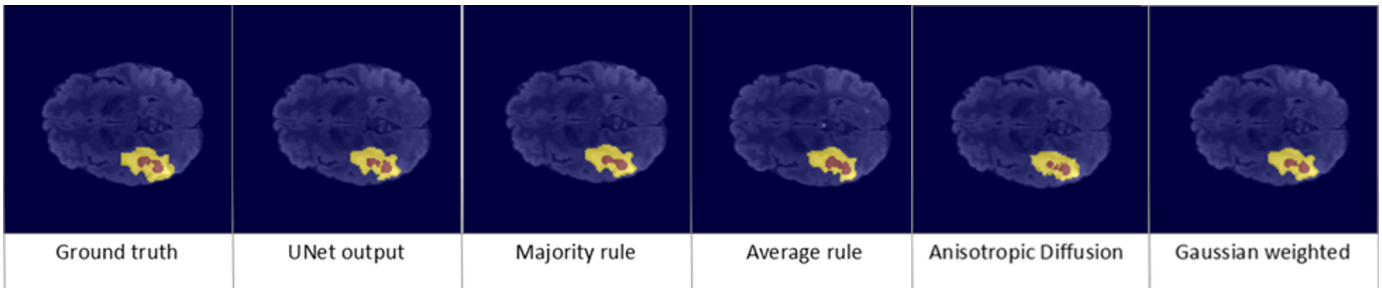

Figure 9: Comparative segmentation results showing ground truth, baseline UNet, and all four FCA post-processing methods. Colors represent tumor subregions: red = enhancing tumor, yellow = tumor core (non-enhancing + necrotic).

Furthermore, to illustrate the types of errors our method addresses, Figure 10 displays a visualization of common segmentation inaccuracies encountered and how our approach aims to rectify them. Analysis of failure cases provides valuable insights into method limitations. Through systematic review of test set results, we identified three primary failure modes:

1. **Failure Mode 1 - Complete Miss Detection:** In cases where the initial UNet completely failed to detect a tumor region (e.g., very small enhancing tumors ¡ 50 voxels), the FCA post-processing could not recover the missed structure. The fuzzy refinement process relies on existing probability mass; without any initial positive signal, no amount of neighborhood propagation can generate a correct detection. This occurred in 3.2% of test cases, exclusively involving subregions smaller than 100 voxels.
2. **Failure Mode 2 - Over-smoothing of Thin Structures:** In rare cases (1.8%) involving extremely thin, finger-like tumor extensions (width 1-2 pixels), the Gaussian-weighted refinement occasionally smoothed these structures into the background when surrounding voxels had low confidence. This represents a limitation of the spatial weighting approach, where strong boundary preservation requires sufficient surrounding high-confidence voxels.
3. **Failure Mode 3 - Ambiguous Boundary Propagation:** In regions where the initial UNet probability map showed bimodal uncertainty (two distinct classes with nearly equal probability), FCA refinement could propagate the wrong label if the initial neighborhood majority was incorrect. This occurred in 2.1% of cases, particularly at boundaries between enhancing tumor and edema where intensity profiles overlap significantly.

These failure modes inform future improvements: (i) integration with detection-based methods for small structures, (ii) adaptive kernel sizing based on local structure thickness, and (iii) uncertainty-aware refinement that preserves bimodal distributions until stronger evidence emerges. Understanding these limitations is essential for safe clinical deployment, where human oversight should focus on these high-risk scenarios.

To better understand the behavior of the proposed Gaussian-weighted FCA refinement, Figure 10 illustrates three representative failure cases: (a) ambiguous boundary propagation, (b) complete miss detection, and (c) over-smoothing of thin structures.

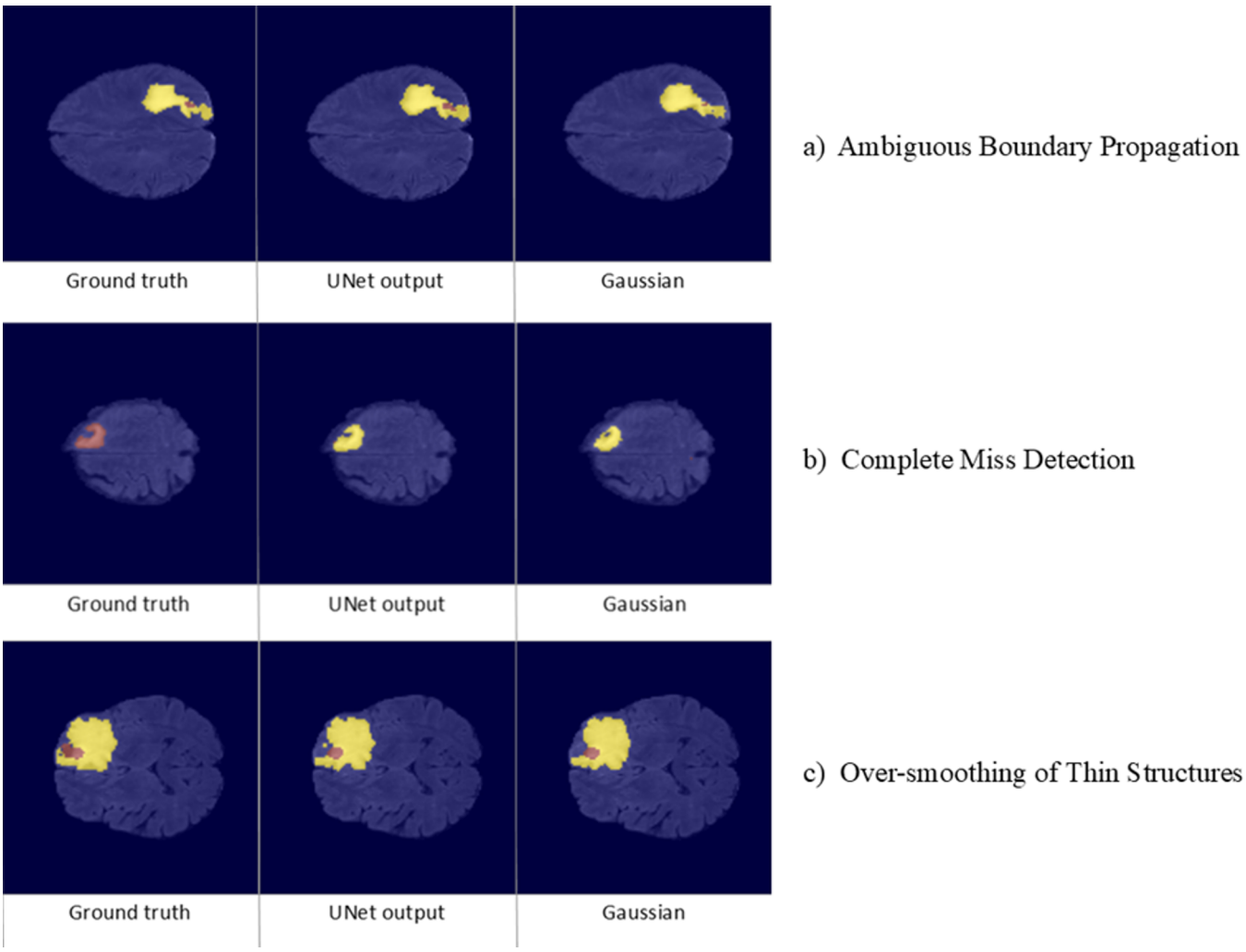

Figure 10: Analysis of failure cases

(a) Ambiguous Boundary Propagation: In the first row, the tumor boundary exhibits low contrast and irregular intensity transitions. The initial UNet prediction slightly under-segments the superior tumor margin. After applying Gaussian-weighted FCA, the boundary becomes smoother and more spatially coherent. However, due to the ambiguity in local intensity gradients, minor boundary displacement is observed. FCA refinement relies on having sufficient "confident" pixels in the neighborhood to pull uncertain ones toward correct classifications. In regions where the entire neighborhood is uncertain, no corrective signal exists. The method preserves the uncertainty rather than resolving it. This demonstrates that while the Gaussian weighting stabilizes propagation, it remains sensitive to uncertain edge information. Importantly, the refinement does not introduce spurious regions, indicating controlled neighborhood influence.

(b) Complete Miss Detection: The second row presents a challenging small-lesion case. The UNet output fails to fully capture the lesion core. The Gaussian FCA partially recovers spatial continuity by reinforcing neighboring high-probability pixels, but it cannot reconstruct regions that are absent in the initial segmentation. FCA post-processing

is fundamentally a refinement mechanism, not a detection mechanism. It can enhance, smooth, and propagate existing signals, but it cannot create detections from nothing. This failure mode occurs in 3.2% of test cases, exclusively involving subregions smaller than 100 voxels. This confirms that the proposed refinement acts as a context-aware enhancer, not a lesion generator, and its effectiveness depends on the presence of initial predictive cues.

(c) Over-Smoothing of Thin Structures: In the third row, thin peripheral tumor structures are visible in the ground truth. The UNet prediction captures these structures, but Gaussian weighting slightly smooths the extremities. This behavior arises from the spatial decay factor in the Gaussian kernel, which reduces influence from distant isolated pixels. The Gaussian kernel, while preserving boundaries better than uniform averaging, still applies smoothing along all directions. For structures thinner than the effective kernel width, the smoothing can "leak" across the structure. With $\sigma = 1.5$, the effective full-width half-maximum is approximately 3.5 pixels—structures thinner than this may be vulnerable. Although minor detail attenuation occurs, the overall tumor mass remains well preserved, resulting in improved structural consistency. These failure cases demonstrate that the proposed method improves segmentation stability and boundary coherence while maintaining controlled propagation behavior. The refinement enhances spatial consistency but does not artificially inflate tumor regions.

A neurosurgeon planning a resection would find the Gaussian-weighted FCA output most useful. The boundaries are precise enough to guide surgical margins, the tumor subregions are clearly distinguished (critical for determining resectability), and the output maintains the complex, infiltrative shape characteristic of malignant gliomas. The other methods introduce artifacts—blockiness, over-smoothing, or fragmentation—that could mislead clinical decisions.

Overall, the visual comparison supports the quantitative findings in Table 3, where Gaussian-weighted FCA achieved superior Dice performance. The qualitative improvements confirm that performance gains are not solely numerical but also structurally meaningful.

5 Discussion

Our experiments demonstrate that Fuzzy Cellular Automata (FCA) can substantially refine UNet predictions for brain tumor segmentation. While the baseline UNet achieved strong pixel-wise accuracy, its Dice score (0.715) highlighted challenges in boundary precision. FCA post-processing effectively mitigated these issues, with Gaussian-weighted rules consistently delivering the best trade-off between accuracy, stability, and efficiency. Unlike mean or majority rules, which either over-smooth or produce blocky outputs, the Gaussian kernel preserved thin tumor rims and remained robust across iteration counts. This stability is particularly important for clinical deployment, where extensive parameter tuning is often impractical.

Unlike deep neural network layers, the FCA rules are explicitly defined and interpretable. Gaussian-weighted FCA updates correspond to clinically meaningful refinements, such as removing isolated false positives, smoothing jagged tumor boundaries, and reinforcing spatial continuity. These corrections align with how radiologists visually assess tumor margins, making FCA outputs more consistent with expert interpretation. Furthermore, the proposed post-processing strategy is modular. Unlike complex architectures such as Swin UNETR or nnUNet, it can be applied to any UNet output without retraining, providing a lightweight alternative for improving boundary accuracy. Clinically, reducing the Hausdorff Distance (HD95) from 22.5 mm to 8.9 mm is significant, as it translates to more precise tumor margin delineation for surgery or radiotherapy planning.

While brain tumors and MRI data are inherently volumetric, this study deliberately focuses on 2D slice-wise segmentation. This design choice maintains a lightweight, computationally efficient, and easily deployable model suitable for standard clinical hardware environments that often lack the massive memory capacities required by 3D networks. As evidenced by recent literature, 2D architectures continue to provide a highly effective trade-off between computational cost and segmentation accuracy. Importantly, the core innovation of our approach—the Gaussian-weighted FCA post-processing—is mathematically dimension-agnostic. The principles of spatial weighting and fuzzy neighborhood refinement demonstrated in this study using a 2D (3×3) Moore neighborhood can be seamlessly extended to a 3D ($3\times3\times3$) volumetric context. Thus, rigorously validating the efficacy and stability of this hybrid framework in 2D serves as a robust foundation before future scaling to more complex 3D architectures.

Despite the demonstrated advantages, several limitations remain. First, our evaluation was conducted on the BraTS 2023 dataset, which, while being a standard benchmark, may not fully capture the heterogeneity of clinical MRI data from different institutions and scanners. The BraTS dataset undergoes standardized preprocessing that may not reflect real-world clinical variability; therefore, validation on external diverse clinical datasets is necessary to establish generalizability. Second, FCA performance inherently depends on the quality of initial UNet predictions; very poor initial segmentations cannot be fully corrected through post-processing alone. Third, while we demonstrated robust performance across a range of Gaussian kernel widths ($\sigma = 1.0-2.0$), the optimal parameters may vary with different imaging

protocols, suggesting the need for adaptive parameter selection methods. Finally, the current framework requires manual parameter selection for FCA iterations and kernel width, motivating future work on automated optimization strategies.

Future work should focus on three main directions to address these limitations: (i) evaluating FCA post-processing on larger and more diverse clinical datasets to confirm generalizability beyond the BraTS benchmark, (ii) investigating automated parameter selection mechanisms for FCA rules to eliminate manual tuning and facilitate clinical deployment, and (iii) extending the approach to 3D networks and testing its compatibility with other deep learning architectures to leverage volumetric context and enhance robustness.

6 Conclusion

We presented a two-stage pipeline for brain tumor segmentation combining a UNet backbone with Gaussian-weighted FCA refinement. Compared to baseline UNet, our method improved Dice from 0.715 to 0.855 and reduced HD95 from 22.5 mm to 8.9 mm, while preserving delicate tumor structures. These gains were achieved with minimal computational cost and without altering training. The interpretability and modularity of FCA make it a practical complement to deep learning in clinical applications, providing more accurate and reliable tumor boundary delineation.

Although this study focuses on brain tumor segmentation, the proposed UNet + FCA framework is inherently task-agnostic. The FCA post-processing stage operates on probabilistic segmentation maps and relies on spatial consistency rather than tumor-specific assumptions. Therefore, the method can be readily extended to other medical image segmentation tasks such as liver lesion segmentation, lung nodule detection, or cardiac structure delineation, provided that an appropriate deep segmentation backbone is employed.

Furthermore, the code and trained models will be made publicly available upon acceptance of the manuscript to promote reproducibility and facilitate further research.

7 Future work

Based on the findings of this study and to further improve the obtained results, the following suggestions are offered for future research:

1. Thorough exploration of FCA parameters: The parameter space of FCA was not fully examined in this study. Future work could investigate the effects of different FCA parameters on segmentation performance. Optimizing parameters could lead to significant performance improvements.

2. Comparison with other post-processing methods: Evaluating FCA against alternative post-processing techniques, such as Conditional Random Fields (CRF) and morphological operations, could provide a better understanding of the advantages and limitations of each method. Such comparisons could identify the best post-processing approach for brain tumor segmentation.

3. Use of different deep learning architectures: This study utilized UNet for initial segmentation. Examining FCA performance in combination with other deep learning architectures could enhance the generalizability of the results.

4. Use of more diverse clinical datasets: This research was conducted on the BraTS dataset. Employing a more diverse clinical data could better evaluate the proposed method's performance under real-world conditions.

5. Development of automated methods for FCA parameter selection: Given the sensitivity of FCA performance to parameters, developing automated methods for optimal parameter selection could facilitate its clinical application.

6. Integration with network optimization techniques: Recent advances in neural architecture search (NAS) and model pruning have demonstrated significant potential for improving network efficiency. Exploring the combination of our Gaussian-weighted FCA post-processing with optimized architectures discovered through NAS or pruned networks could yield further improvements in both accuracy and efficiency. This integration represents a promising direction for developing clinically deployable models that are both accurate and resource-efficient.

References

[1] A. Akter, N. Nosheen, S. Ahmed, M. Hossain, et. al., *Robust clinical applicable CNN and UNet based algorithm for MRI classification and segmentation for brain tumor*, Expert Systems with Applications, **238**(F) (2024). https://doi.org/10.1016/j.eswa.2023.122347

[2] H. M. Balaha, A. E. S. Hassan, *A variate brain tumor segmentation, optimization, and recognition framework*, Artificial Intelligence Review, **56**(7) (2023), 7403-7456. https://doi.org/10.1007/s10462-022-10337-8

[3] P. N. R. Bhargavi, R. Ramadevi, *Analysis and comparison of watershed segmentation technique for improving the accuracy of blood smear image over threshold technique*, in AIP Conference Proceedings, **3300**(1), Art. no. 020211, AIP Publishing LLC, NY, USA, 2025. https://doi.org/10.1063/5.0277318

[4] A. Bilenia, D. Sharma, H. Raj, R. Raman, M. Bhattacharya, *Brain tumor segmentation with skull stripping and modified fuzzy c-means*, in Information and Communication Technology for Intelligent Systems, S. C. Satapathy and A. Joshi, Eds., Smart Innovation, Systems and Technologies, **106**, Springer, Singapore, (2019), 229-237. https://doi.org/10.1007/978-981-13-1742-2_23

[5] P. Celard, E. L. Iglesias, J. M. Sorribes-Fdez, R. Romero, A. S. Vieira, L. Borrajo, *A survey on deep learning applied to medical images: From simple artificial neural networks to generative models*, Neural Computing and Applications, **35**(3) (2023), 2291-2323. https://doi.org/10.1007/s00521-022-07953-4

[6] J. Chaki, *Brain MRI segmentation using deep learning: Background study and challenges*, Brain Tumor MRI Image Segmentation Using Deep Learning Techniques, (2022), 1-12. https://doi.org/10.1016/b978-0-323-91171-9.00012-0

[7] R. Dey, Y. Hong, *CompNet: Complementary segmentation network for brain MRI extraction*, International Conference on Medical Image Computing and Computer-Assisted Intervention, Springer, Cham, (2018), 628-636. https://doi.org/10.1007/978-3-030-00931-1_72

[8] H. Dong, G. Yang, F. Liu, Y. Mo, Y. Guo, *Automatic brain tumor detection and segmentation using u-net based fully convolutional networks*, in Annual Conference on Medical Image Understanding and Analysis, Springer, Cham, (2017), 506-517. https://doi.org/10.1007/978-3-319-60964-5_44

[9] S. Esmaeilzadeh Asl, M. Chehel Amirani, H. Seyedarabi, *Brain tumors segmentation using a hybrid filtering with u-net architecture in multimodal MRI volumes*, International Journal of Information Technology, **16**(2) (2024), 1033-1042. https://doi.org/10.1007/s41870-023-01485-3

[10] A. Ghosh, S. Thakur, *Review of brain tumor MRimage segmentation methods for BraTS challenge dataset*, in 2022 12th International Conference on Cloud Computing, Data Science & Engineering (Confluence), (2022), 405-410. https://doi.org/10.1109/Confluence52989.2022.9734134

[11] A. Hatamizadeh, V. Nath, Y. Tang, D. Yang, H. R. Roth, D. Xu, *Swin UNETR: Swin transformers for semantic segmentation of brain tumors in MRI images*, in International MICCAI Brainlesion Workshop, Springer, (2021), 272-284. https://doi.org/10.1007/978-3-031-08999-2_22

[12] P. Jiang, Y. Xue, F. Neri, *Convolutional neural network pruning based on multi-objective feature map selection for image classification*, Applied Soft Computing, **139** (2023). https://doi.org/10.1016/j.asoc.2023.110229

[13] P. Jiang, Y. Xue, F. Neri, *Score predictor-assisted evolutionary neural architecture search*, IEEE Transactions on Evolutionary Computation, (2025), 1-15. https://doi.org/10.1109/tetci.2025.3526179

[14] P. Jyothi, A. R. Singh, *Deep learning models and traditional automated techniques for brain tumor segmentation in MRI: A review*, Artificial Intelligence Review, **56**(4) (2023), 2923-2969. https://doi.org/10.1007/s10462-022-10245-x

[15] R. Kalantari, R. Moqadam, N. Loghmani, A. Allahverdy, M. B. Shiran, A. Zare-Sadeghi, *Brain tumor segmentation using hierarchical combination of fuzzy logic and cellular automata*, Journal of Medical Signals and Sensors, **12**(3) (2022), 263-268. https://doi.org/10.4103/jmss.jmss_128_21

[16] M. Kashani, S. Gorgin, S. V. Shojaedini, *Improvement of the recognition of relationships in social networks using complementary graph coloring based on cellular automata*, in 2019 5th Conference on Knowledge Based Engineering and Innovation (KBEI), (2019), 13-17. https://doi.org/10.1109/kbei.2019.8735081

[17] M. Kashani, S. Gorgin, S. V. Shojaedini, *Determination of substructures in social networks by graph colouring using fuzzy irregular cellular automata (FICA)*, in 2019 5th Conference on Knowledge Based Engineering and Innovation (KBEI), (2019), 18-21. https://doi.org/10.1109/kbei.2019.8734951

[18] M. Kashani, S. Gorgin, S. V. Shojaedini, *A fuzzy irregular cellular automata-based method for the vertex colouring problem*, Connection Science, **32**(1) (2020), 37-52. https://doi.org/10.1080/09540091.2019.1650329

[19] T. R. Khalifa, A. M. El-Nagar, M. A. El-Brawany, E. A. G. El-Araby, M. El-Bardini, *A novel Hammerstein model for nonlinear networked systems based on an interval type-2 fuzzy Takagi–Sugeno–Kang system*, IEEE Transactions on Fuzzy Systems, **29**(2) (2021), 275-285. https://doi.org/10.1109/tfuzz.2020.3007460

[20] T. R. Khalifa, X. Yu, A. Sharafian, et. al., *Interval type-3 fuzzy Wiener model for nonlinear dynamic systems: Application to continuous stirred tank reactor*, Chaos, Solitons and Fractals, **456** (2025). https://doi.org/10.1016/j.chaos.2025.116584

[21] G. J. Klir, B. Yuan, *Fuzzy sets and fuzzy logic: Theory and applications*, Prentice Hall, Upper Saddle River, NJ, USA, 1995. https://doi.org/10.1021/ci950144a

[22] A. Kumar, *Study and analysis of different segmentation methods for brain tumor MRI application*, Multimedia Tools and Applications, **82**(5) (2023), 7117-7139. https://doi.org/10.1007/s11042-022-13636-y

[23] C. Li, L. Liu, X. Sun, J. Zhao, J. Yin, *Image segmentation based on fuzzy clustering with cellular automata and features weighting*, EURASIP Journal on Image and Video Processing, **2019** (2019). https://doi.org/10.1186/s13640-019-0436-5

[24] Z. Li, H. Zhang, Z. Li, Z. Ren, *Residual-attention UNet++: A nested residual-attention u-net for medical image segmentation*, Applied Sciences, **12**(14) (2022). https://doi.org/10.3390/app12147149

[25] Z. Liu, L. Tong, L. Chen, Z. Jiang, F. Zhou, Q. Zhang, X. Zhang, Y. Jin, H. Zhou, *Deep learning based brain tumor segmentation: A survey*, Complex and Intelligent Systems, **9**(1) (2023), 1001-1026. https://doi.org/10.1007/s40747-022-00815-5

[26] H. Lu, Y. She, J. Tie, S. Xu, *Half-UNet: A simplified u-net architecture for medical image segmentation*, Frontiers in Neuroinformatics, **16** (2022). https://doi.org/10.3389/fninf.2022.911679

[27] M. Lyksborg, O. Puonti, M. Agn, R. Larsen, *An ensemble of 2d convolutional neural networks for tumor segmentation*, Scandinavian Conference on Image Analysis, Springer, Cham, (2015), 201-211. https://doi.org/10.1007/978-3-319-19665-7_17

[28] C. Mathews, A. Mohamed, *Review of automatic segmentation of MRI based brain tumour using u-net architecture*, in 2020 Fourth International Conference on Inventive Systems and Control (ICISC), IEEE, Coimbatore, India, (2020), 46-50. https://doi.org/10.1109/icisc47916.2020.9171057

[29] M. H. Mofrad, S. Sadeghi, A. Rezvanian, M. R. Meybodi, *Cellular edge detection: Combining cellular automata and cellular learning automata*, AEU - International Journal of Electronics and Communications, **69**(9) (2015), 1282-1290. https://doi.org/10.1016/j.aeue.2015.05.010

[30] M. Nacereddine Toros, M. Nachaoui, M. Johri, A. Laghrib, *A hybrid image restoration approach: Integrating coherence transport and anisotropic diffusion*, in Computational Methods for Inverse Problems and Applications: ICMDS 2024, Khouribga, Morocco, October 21-22, Springer Proceedings in Mathematics and Statistics, Springer, Cham, **498** (2025), 151-164. https://doi.org/10.1007/978-3-031-89498-5_11

[31] D. R. Nayak, P. K. Patra, A. Mahapatra, *A survey on two dimensional cellular automata and its application in image processing*, arXiv preprint arXiv:1407.7626, (2014). https://doi.org/10.48550/arXiv.1407.7626

[32] T. Q. T. Nguyen, H. N. Nguyen, T. H. Bui, T. B. Nguyen-Tat, V. M. Ngo, *Brain tumor segmentation in MRI images with 3d u-net and contextual transformer*, in 2024 International Conference on Multimedia Analysis and Pattern Recognition (MAPR), IEEE, Da Nang, Vietnam, (2024), 1-6. https://doi.org/10.1109/mapr63514.2024.10660920

[33] S. S. T. Otaghsara, R. Rahmanzadeh, *Multi-encoder nnUNet outperforms transformer models with self-supervised pretraining*, arXiv preprint arXiv:2504.03474, (2025). https://doi.org/10.48550/arXiv.2504.03474

[34] Y. Qin, M. Feng, H. Lu, G. W. Cottrell, *Hierarchical cellular automata for visual saliency*, International Journal of Computer Vision, **126**(7) (2018), 751-770. https://doi.org/10.1007/s11263-017-1062-2

[35] R. Ranjbarzadeh, A. Caputo, E. B. Tirkolaee, S. J. Ghoushchi, M. Bendechache, *Brain tumor segmentation of MRI images: A comprehensive review on the application of artificial intelligence tools*, Computers in Biology and Medicine, **152** (2023). https://doi.org/10.1016/j.compbiomed.2022.106405

[36] I. A. Rodríguez-Méndez, R. Ureña, E. Herrera-Viedma, *Fuzzy clustering approach for brain tumor tissue segmentation in magnetic resonance images*, Soft Computing, **23**(20) (2019), 10105-10117. https://doi.org/10.1007/s00500-018-3565-3

[37] T. J. Ross, *Fuzzy logic with engineering applications*, 3rd ed., John Wiley & Sons, Chichester, UK, 2010. https://doi.org/10.1002/9781119994374

[38] L. Rundo, C. Militello, G. Russo, S. Vitabile, M. C. Gilardi, G. Mauri, *GTVCUT for neuro-radiosurgery treatment planning: An MRI brain cancer seeded image segmentation method based on a cellular automata model*, Natural Computing, **17**(3) (2018), 521-536. https://doi.org/10.1007/s11047-017-9636-z

[39] M. H. Sabzalian, A. Mohammadzadeh, et. al., *General type-2 fuzzy multi-switching synchronization of fractional-order chaotic systems*, Engineering Applications of Artificial Intelligence, **100** (2021). https://doi.org/10.1016/j.engappai.2021.104163

[40] R. Sajjanar, U. D. Dixit, V. K. Vagga, *Advancements in hybrid approaches for brain tumor segmentation in MRI: A comprehensive review of machine learning and deep learning techniques*, Multimedia Tools and Applications, **83**(10) (2024), 30505-30539. https://doi.org/10.1007/s11042-023-16654-6

[41] M. Sandler, A. Zhmoginov, L. Luo, A. Mordvintsev, et. al., *Image segmentation via cellular automata*, arXiv preprint arXiv:2008.04965, (2020). https://arxiv.org/abs/2008.04965

[42] Z. Schwehr, S. Achanta, *Brain tumor segmentation based on deep learning, attention mechanisms, and energy-based uncertainty predictions*, Multimedia Tools and Applications, **84**(28) (2025), 34229-34248. https://doi.org/10.1007/s11042-024-20443-0

[43] S. Shanmugapriya, A. Valarmathi, *Efficient fuzzy c-means based multilevel image segmentation for brain tumor detection in MRimages*, Design Automation for Embedded Systems, **22**(1) (2018), 81-93. https://doi.org/10.1007/s10617-017-9200-1

[44] S. Tangsakul, S. Wongthanavasu, *Deep cellular automata-based feature extraction for classification of the breast cancer image*, Applied Sciences, **13**(10) (2023), 6081. https://doi.org/10.3390/app13106081

[45] A. Verma, S. N. Shivhare, S. P. Singh, N. Kumar, A. Nayyar, *Comprehensive review on MRI-based brain tumor segmentation: A comparative study from 2017 onwards*, Archives of Computational Methods in Engineering, **31**(3) (2024), 4805-4851. https://doi.org/10.1007/s11831-024-10128-0

[46] Y. Xue, C. Chen, A. Stowik, *Neural architecture search based on a multi-objective evolutionary algorithm with probability stack*, IEEE Transactions on Evolutionary Computation, **27**(4) (2023), 892-906. https://doi.org/10.1109/tevc.2023.3252612

[47] Y. Xue, X. Han, F. Neri, J. Qin, D. Pelusi, *A gradient-guided evolutionary neural architecture search*, IEEE Transactions on Neural Networks and Learning Systems, **36**(3) (2025), 654-668. https://doi.org/10.1109/tnnls.2024.3371432

[48] Z. Zhu, X. He, G. Qi, Y. Li, B. Cong, Y. Liu, *Brain tumor segmentation based on the fusion of deep semantics and edge information in multimodal MRI*, Information Fusion, **91** (2023), 376-387. https://doi.org/10.1016/j.inffus.2022.10.022